PAPER

Check for updates

Exploiting perylene- and naphthalene-based planar aromatic n-type dopants for SWCNT cathodes in inverted perovskite solar cells

Achmad Syarif Hidayat, [iD] [a] Naoki Ueoka,[a] Hisayoshi Oshima,[b] Yoshimasa Hijikata[c] and Yutaka Matsuo [iD] *[ab]

Inverted perovskite solar cells (PSCs) with planar p–i–n architecture offer enhanced stability and tandem compatibility. However, their performance remains constrained by the instability and rigidity of conventional metal cathodes. Single-walled carbon nanotubes (SWCNTs) have emerged as promising alternatives owing to their conductivity, flexibility, and processability. However, their intrinsic p-type nature and low work function relative to the perovskite conduction band limit their applicability as cathodes in PSCs. To overcome these challenges, we employed a molecular doping strategy using planar aromatic n-type dopants, to modulate the electronic properties of SWCNTs. Three π-conjugated imide-based molecules N,N'-bis[3-(dimethylamino)propyl]perylene-3,4,9,10-tetracarboxylic diimide (PDIN), its bay-substituted dibromo derivative, N,N'-bis[3-(dimethylamino)-propyl]-1,7-dibromoperylene-3,4,9,10-tetracarboxyl diimide ($PDINBr_2$), and the naphthalene analogue N,N'-bis[3-(dimethylamino) propyl]naphthalene-1,4,5,8-tetracarboxylic diimide (NDIN) were selected for their tunable LUMO levels, high intrinsic conductivity, and strong $\pi-\pi$ interactions with SWCNTs. Density functional theory (DFT) calculations reveal that $PDINBr_2$ doped SWCNTs exhibited the formation of new unoccupied states favorable for efficient charge transfer from the electron transporting layer (ETL), supported by stable adsorption and strong orbital overlap. The doped SWCNTs were integrated as cathodes in inverted PSCs, achieving power conversion efficiencies up to 10.12%. Device characterization confirmed improved electron extraction, extended carrier lifetime, and suppressed interfacial recombination. Moreover, perylene-based dopants contributed to enhanced device stability, with unencapsulated cells retaining 80% of their initial efficiency after 800 hours under ambient light and 25% relative humidity. This work demonstrates a new strategy to use planar aromatic molecular dopants for enabling SWCNTs as cathodes and provides a pathway for scalable, metal-free electrodes in next-generation PSCs.

Broader context

The rapid advancement of photovoltaic technologies has emphasized the need for next generation electrodes that combine excellent electrical properties with long-term chemical durability. Carbon nanomaterials, particularly single-walled carbon nanotubes (SWCNTs), have emerged as promising candidates, offering advantages over conventional metal electrodes such as gold, silver, and copper, which are prone to interlayer diffusion and chemical degradation. While SWCNTs are widely used as anodes, their intrinsic p-type character limits their direct application as cathodes in perovskite solar cells (PSCs). Here, we present a molecular doping strategy using perylene- and naphthalene-based aromatic compounds (PDIN, $PDINBr_2$, NDIN) to produce n-type SWCNT electrodes suitable for cathodes in PSCs. They offer distinct advantages, including strong $\pi-\pi$ interactions and favourable energy level alignment to the electron-transporting layer, which enable effective charge transfer. The cathode exhibits enhanced open-circuit voltage and fill factor, achieving power conversion efficiencies up to 10.12% with improved operational stability. This work establishes a sustainable, metal-free approach toward flexible and durable carbon-based cathodes for next-generation photovoltaic technologies.

Introduction

Inverted perovskite solar cells (PSCs) employing planar p–i–n architecture have gained considerable attention due to their enhanced stability, reduced hysteresis, and suitability for tandem applications.[1,2] Metal electrodes are commonly used as cathodes in PSCs,[3–5] but they suffer from degradation and poor compatibility with flexible or roll-to-roll fabrication.[6–8] To

[a]Department of Chemical Systems Engineering, Graduate School of Engineering, Nagoya University, Nagoya, Aichi, Japan. E-mail: matsuo.yutaka.h7@f.mail. nagoya-u.ac.jp

[b]Institute of Materials Innovation, Institutes of Innovation for Future Society, Nagoya University, Nagoya, Aichi, Japan

[c]Advanced Research and Innovation Center, Denso Corporation, Kariya, Aichi, Japan

address these issues, single-walled carbon nanotubes (SWCNTs) have emerged as promising alternatives, offering high electrical conductivity, chemical stability, mechanical flexibility, and tuneable optical transparency.[9–11] However, their utilization has been primarily explored as anodes due to their p-type nature inducing low work function (−4.7 to −5 eV), which has favourable alignment with the perovskite valence band.[12–20] This limits their direct application as cathodes in PSCs.[21,22] One approach to increase the SWCNT work function is by employing molecular n-type doping. Organic n-type dopants such as dimethyl-dihydro-benzo imidazoles,[23] tetramethyl guanidino-benzene,[24] viologens,[25] and organorhodium dimers[26] effectively reduced the SWCNT work function and improved electron injection in CNT-based field-effect transistors. Moreover, such doping strategies were also used to tune the conductivity and charge transfer properties in CNT-based chemical sensors and photocatalysts.[27,28] While molecular n-type doping of SWCNTs has been extensively explored to tune their electronic properties for a wide range of technologies, their application as cathodes in PSCs remains largely unexplored.

In this work we explored the use of perylene- and naphthalene-based planar aromatic dopants, N,N′-bis[3-(dimethylamino)propyl]perylene-3,4,9,10-tetracarboxylic di-imide (PDIN), its bay-substituted dibromo derivative, N,N′-bis[3-(dimethylamine)-propyl]-1,7-dibromoperylene-3,4,9,10-

tetracarboxyl diimide (PDINBr$_2$), and their naphthalene analogue N,N′-bis[3-(dimethylamino)propyl]naphthalene-1,4,5,8-tetracarboxylic diimide (NDIN) as n-type dopants for SWCNT cathodes in inverted PSCs. Previously, perylene diimide (PDI) derivatives have been extensively explored as efficient electron-transporting and cathode interlayer materials in inverted solar cells. For example, Gao et al. developed a D–A–D fused-ring PDI cathode interface layer for inverted PSCs, achieving a power conversion efficiency of 24.64% by simultaneously improving energy-level alignment and interfacial charge extraction.[29] Wang and co-workers further designed selenophene-fused PDI and naphthodithiophene diimide (NDTI) cathode interlayers, enabling ≈19% efficiency in binary organic solar cells via enhanced electron extraction at the cathode interface.[30,31] However, most of these studies employ PDI-type molecules as continuous thin-film interlayers on transparent conductive oxide (TCO) or metal electrodes, whereas the use of PDIN-type derivatives as n-type dopants for nanocarbon networks such as SWCNT cathodes in perovskite solar cells remains largely unexplored.

Perylene- and naphthalene-based planar aromatic dopants were selected due to their high intrinsic conductivity with large planar π-conjugated backbones that facilitate strong π–π stacking with SWCNTs and promoting effective charge transfer at low doping concentrations.[32–34] Importantly, their energy
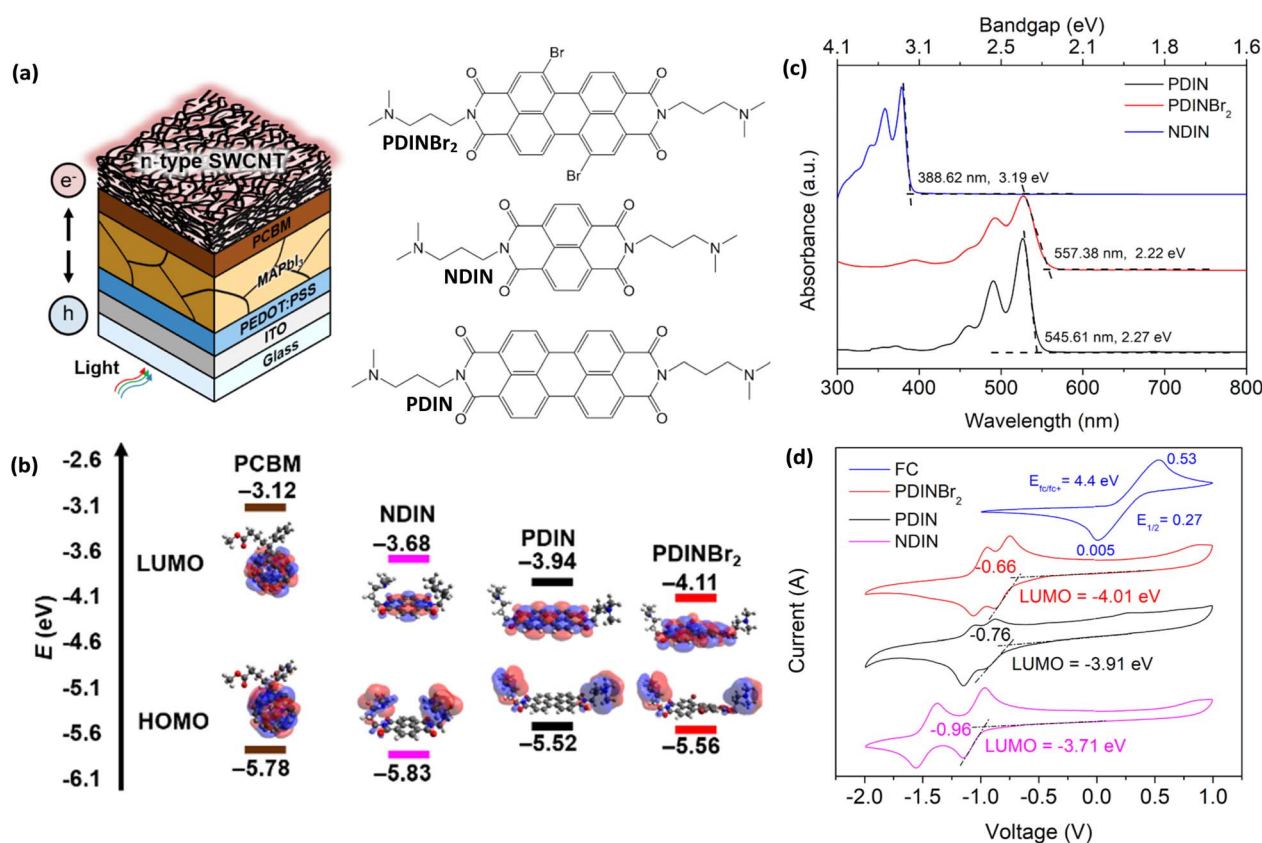

Fig. 1 (a) Device architecture of an inverted PSC utilizing a PDIN/PDINBr$_2$/NDIN doped SWCNT cathode, (b) DFT calculated HOMO–LUMO energy of PCBM, NDIN, PDIN, and PDINBr$_2$, (c) UV-vis spectra of PDIN, PDINBr$_2$, and NDIN measured in TFE and (d) their cyclic voltammetry plot in 0.1 M NBu$_4$PF$_6$/ODCB, with Fc/Fc$^+$ as the internal reference.

levels can be chemically tuned *via* core or end-group modification to match the conduction band levels of perovskites and ETL.[35,36] Using DFT calculations, we investigated how these dopants influence the electronic structure of SWCNTs. Perylene- and naphthalene-cores exhibited strong unoccupied molecular orbital overlap with the SWCNT sidewalls. Notably, PDIN and PDINBr$_2$ doped SWCNTs showed favourable lowest unoccupied molecular orbital (LUMO) alignment to accept electrons from PCBM. Stable adsorption *via* π–π interactions induced electron transfer and larger dipole moment oriented toward the nanotube surface. In contrast, NDIN doped SWCNTs exhibited mismatched energy with PCBM and induced less efficient charge transfer.

We implemented these doped SWCNTs as the cathode in inverted perovskite solar cells [glass/ITO/PEDOT:PSS/MAPbI$_3$/PCBM/n-doped SWCNTs] (Fig. 1a) and analysed their impact on device performance. The PDINBr$_2$ doped SWCNT cathode collected electrons efficiently with the best-performing devices achieving a power conversion efficiency (PCE) of 10.12%. Carrier lifetime measurements revealed a faster interfacial charge transfer from the perovskite to the ETL with prolonged exciton lifetime in the bulk. Owing to their larger aromatic core and hydrophobic nature, the perylene-based dopant contributed to enhanced device stability, with unencapsulated PSCs retaining 80% of their initial efficiency after approximately 800 hours of storage under controlled temperature (25 °C), humidity (25% RH) and ambient light (300 lux) conditions. This work highlights the potential of a molecular n-type doping strategy for enabling the utilization of SWCNTs as cathodes in inverted PSCs.

Results and discussion

Perylene, naphthalene tetracarboxylic diimide, and their derivatives offer some significant advantages as n-type dopants for SWCNT cathodes in inverted PSC devices. Both LUMO levels of the individual dopants and their SWCNT complexes lie below the PCBM. DFT calculations showed the molecular orbital of the individual dopants compared to PCBM (Fig. 1b). PDINBr$_2$ showed the lowest LUMO among all dopants, while the smaller conjugated systems like naphthalene led to higher LUMO levels. These findings were supported by experimental results from UV-Vis spectroscopy and cyclic voltammetry (Fig. 1c and d). The onset reduction potentials and optical band gaps exhibited consistent trends, with PDINBr$_2$ showing the highest reduction potential relative to Fc/Fc$^+$ with the smallest optical band gap among all dopants.

We further investigated the adsorption properties of n-dopants on the SWCNT surface and analyzed their electronic structures. DFT calculations were first conducted to model and optimize the adsorption of each dopant on a semiconducting (5,0) SWCNT. The results revealed stable non-covalent interactions *via* π–π stacking between the aromatic systems with intermolecular distances in the range of 3.9–4.3 Å. The calculated adsorption energies followed the order PDINBr$_2$ (−0.11 eV) > PDIN (−0.08 eV) > NDIN (−0.05 eV). Notably, these interactions induced significant dipole moments, which
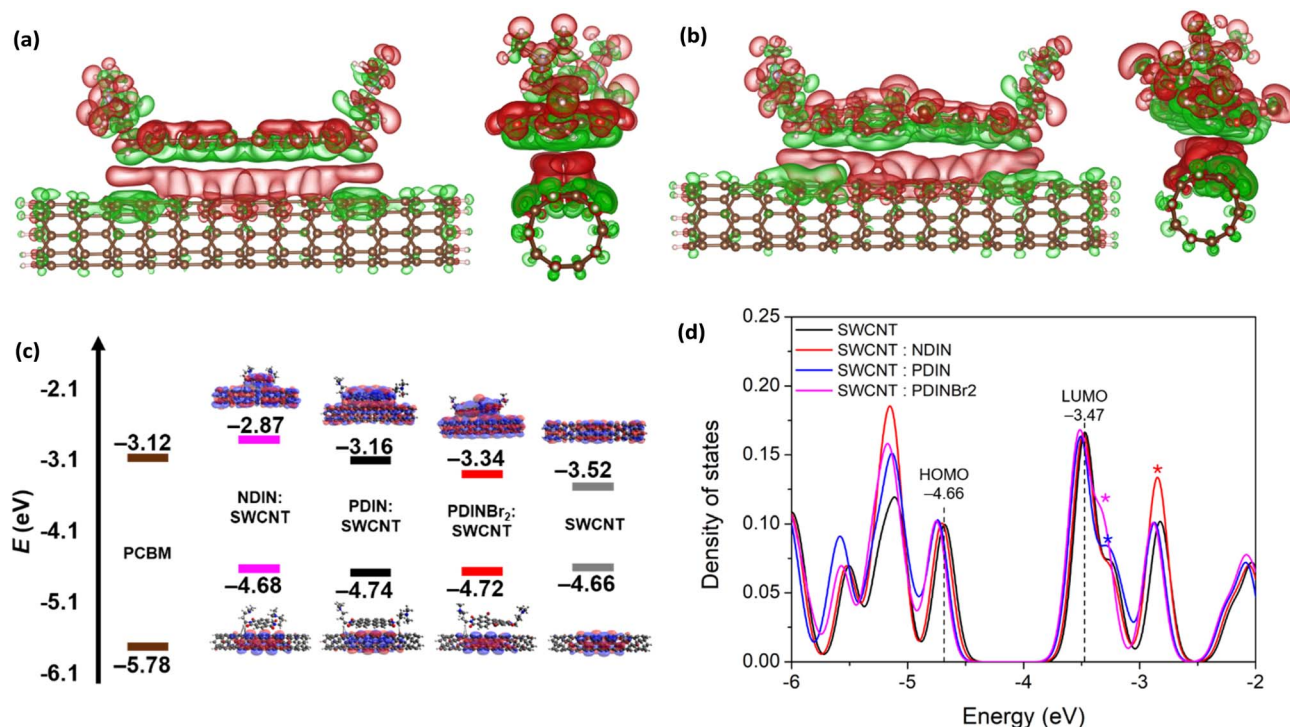

Fig. 2 Iso-surface of charge density difference when (a) PDINBr$_2$ or (b) PDIN was adsorbed on a semiconducting (5,0) SWCNT. Red and green regions represent electron accumulation and depletion, respectively. (c) Molecular orbital distributions of the SWCNT–dopant complexes, and (d) their density of states (DOS) showing the emergence of new unoccupied states near the conduction band edge.

followed the same order, $PDINBr_2$ (1.73 D) > PDIN (1.44 D) > NDIN (0.39 D). This trend indicated some change of charge distribution along the SWCNT surface upon molecular adsorption.

Charge density difference analysis showed electron accumulation near the SWCNT sidewalls (red regions) and electron depletion near the dopant cores (green regions), indicating extensive electron transfer from the dopants to the nanotube *via* π–π interactions between the aromatic system (Fig. 2a and b). The distribution of electron accumulation was influenced by the relative planarity of the dopant cores with respect to the SWCNT surface. Notably, $PDINBr_2$ adopted a slightly tilted geometry, enabling better curvature conformity and broader surface contact with the SWCNT sidewall. Hirshfeld atomic charge and population analysis quantified the transferred charge, where $PDINBr_2$ induced the greatest charge transfer ($0.09e$), followed by PDIN ($0.08e$), and NDIN ($0.02e$) (Table S1).

Orbital analysis revealed that the LUMO of the doped SWCNTs is delocalized over both the dopant aromatic system and the SWCNTs (Fig. 2c). The total density of states (TDOS) diagram showed the emergence of new unoccupied states, indicated by asterisk marks, overlapping with the conduction band of the SWCNTs at varying energy levels (Fig. 2d). $PDINBr_2$ showed the most pronounced population nearest to the SWCNT's LUMO. This suggested strong electronic interaction between dopants and SWCNTs, in which these states likely originate from orbital hybridization of each conduction band. Partial density of states (PDOS) was analysed by decomposing orbital contributions from the SWCNT sidewall (aligned parallel to the dopant core), SWCNT terminal, dopant core, and the dopant terminal end (Fig. S1). The results clearly indicate that the newly emerged unoccupied states originated from the core region of each dopant molecule. The localization of the LUMO on the dopant suggests a possible charge transfer pathway in which, upon electron transfer from PCBM, the SWCNT dopant complexes can transiently accommodate the charge. Among all dopants, PDIN and $PDINBr_2$ doped SWCNTs exhibited LUMO energy levels (−3.16 and −3.34 eV) lower than that of PCBM. This alignment may induce a more efficient charge transfer process than the NDIN doped SWCNTs which have a slightly higher LUMO energy than PCBM.

We evaluated the Seebeck coefficient (S) of the doped SWCNT films. The dopants were incorporated into the intertwined, densely packed SWCNT networks (Fig. 3a). Noticeable negative shifts in S were observed, confirming its n-type characteristic. $PDINBr_2$ yielded the most negative Seebeck value
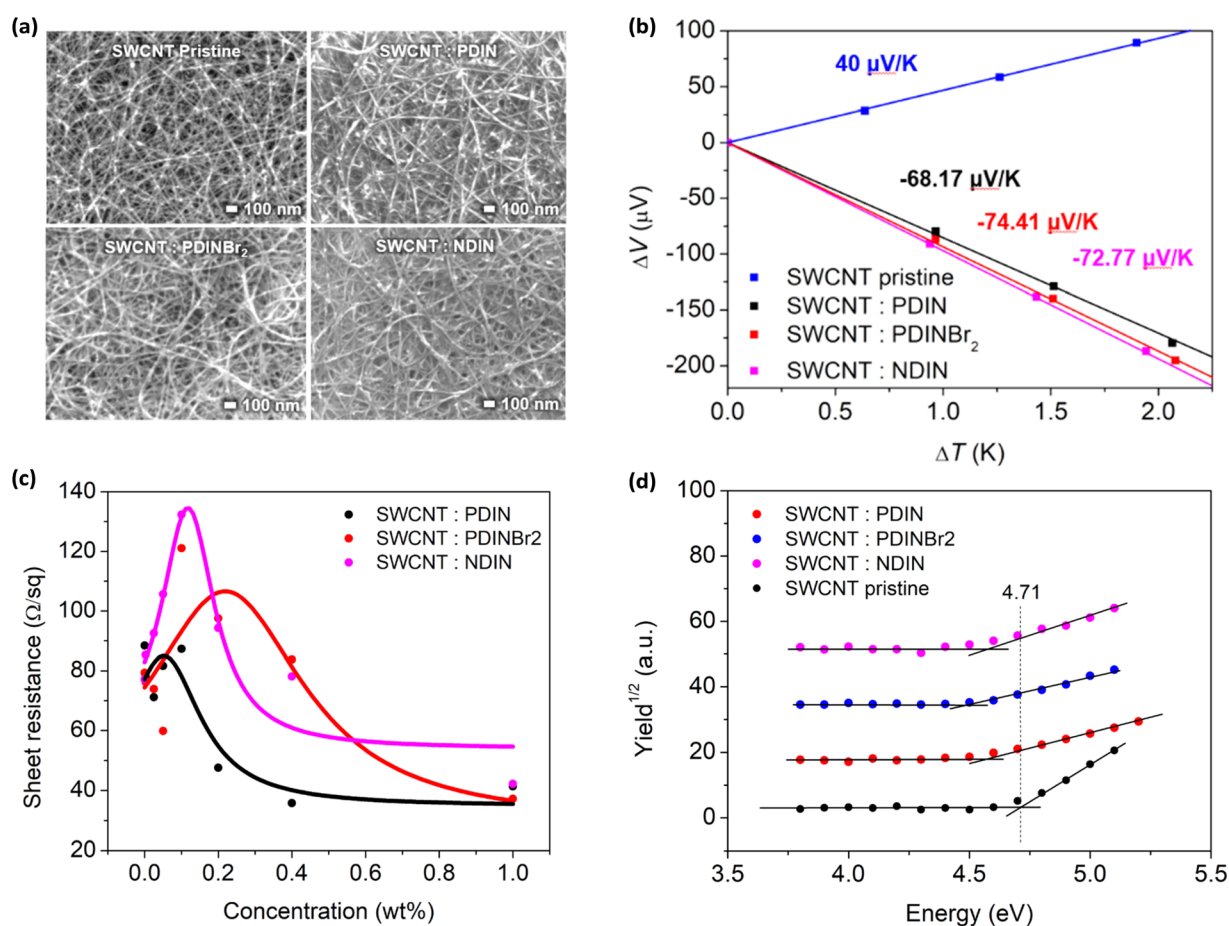

Fig. 3 (a) SEM images of pristine and doped SWCNT film, (b) plots of thermoelectric voltage (ΔV) *versus* the applied temperature difference (ΔT) of pristine and doped SWCNT films, (c) correlation between sheet resistance and doping concentration in SWCNT films, and (d) PYSA spectra of pristine and doped SWCNT films.

(-74.41 μV K^{-1}), followed by NDIN (-72.77 μV K^{-1}) and PDIN (-68.17 μV K^{-1}) (Fig. 3b). The successful n-type doping was also confirmed by NIR absorption and Raman spectroscopy. In the NIR region, a significant bleaching of the S$_{11}$ and S$_{22}$ bands was observed upon doping, indicating electron injection into the semiconducting SWCNTs near the conduction band in the complex. In addition to bleaching, the absorption peaks exhibited a redshift due to the reduced band gap upon doping (Fig. S2). Raman spectra further supported this finding, where the G$^-$ band exhibited broadening and a downshift, typical of increased electron density and modulation of the tangential vibrational modes (Fig. S3).

Prior to utilizing the n-type SWCNT films as the cathode in a PSC, we first determined the appropriate doping concentration by screening the sheet resistance (R_{Sheet}) of the doped SWCNT films over a range of doping concentrations (Fig. 3c). An initial increase in R_{Sheet} was observed at low doping concentrations, indicating that intrinsic p-type carriers were being compensated by the introduced n-type dopants. The resistance reached a maximum at around 0.1–0.2 wt%, suggesting the charge neutrality point where hole and electron populations are balanced. Beyond 1 wt%, R_{Sheet} decreased significantly initially from 80 Ω sq^{-1} (pristine) to 41.33 Ω sq^{-1} (SWCNTs:PDIN), 37.21 Ω sq^{-1} (SWCNTs:PDINBr$_2$), and 42.19 Ω sq^{-1} (SWCNTs:NDIN). The carrier mobility (μ) of the SWCNT film also increased significantly upon doping, initially from 1.64×10^{-2} cm^2 V^{-1} s^{-1} (pristine), to 6.11×10^{-2} cm^2 V^{-1} s^{-1} (SWCNTs:PDINBr$_2$), 3.70×10^{-2} cm^2 V^{-1} s^{-1} (SWCNTs:PDIN), and 4.54×10^{-2} cm^2 V^{-1} s^{-1} (SWCNTs:NDIN) (Fig. S4). The mobility values exhibited only marginal changes when exposed to light, indicating that the doping effect is stable under illumination (Fig. S5). Importantly, substantial reductions in work function (ϕ) were observed, shifting from 4.71 eV (pristine) to 4.57 eV (PDIN), 4.46 eV (PDINBr$_2$), and 4.53 eV (NDIN) (Fig. 3d), resulting in improved energy level alignment with the PCBM. These enhancements in electrical conductivity and energy alignment are beneficial to facilitate efficient electron extraction in inverted PSCs.

The inverted PSC comprising of glass/ITO/PEDOT:PSS/MAPbI$_3$/PC$_{60}$BM/n-doped SWCNTs was fabricated. MAPbI$_3$ was employed due to its highly reproducible films under our processing conditions. Although FA-rich perovskites can deliver higher record efficiencies with meticulous compositional and additive engineering,[37–40] in this work we focus on reproducibly isolating the effects of n-doped SWCNT electrodes using MAPbI$_3$. The energy level diagram and corresponding device structure were constructed based on photoelectron yield spectroscopy in air (PYSA), cyclic voltammetry (CV), and UV-Vis absorption measurements (Fig. 4a). Favorable energy alignment was confirmed for PDIN and PDINBr$_2$, where electron transfer favorably occurred from the conduction band minimum of MAPbI$_3$ (-3.8 eV) to PCBM (LUMO -3.9 eV), then to the dopant LUMO (-3.91 to -4.01 eV), and finally into the conduction states of the SWCNTs. Cross-sectional SEM images confirm a uniform layer structure, with the doped SWCNT films conformally covering the underlying PCBM layer (Fig. 4b).
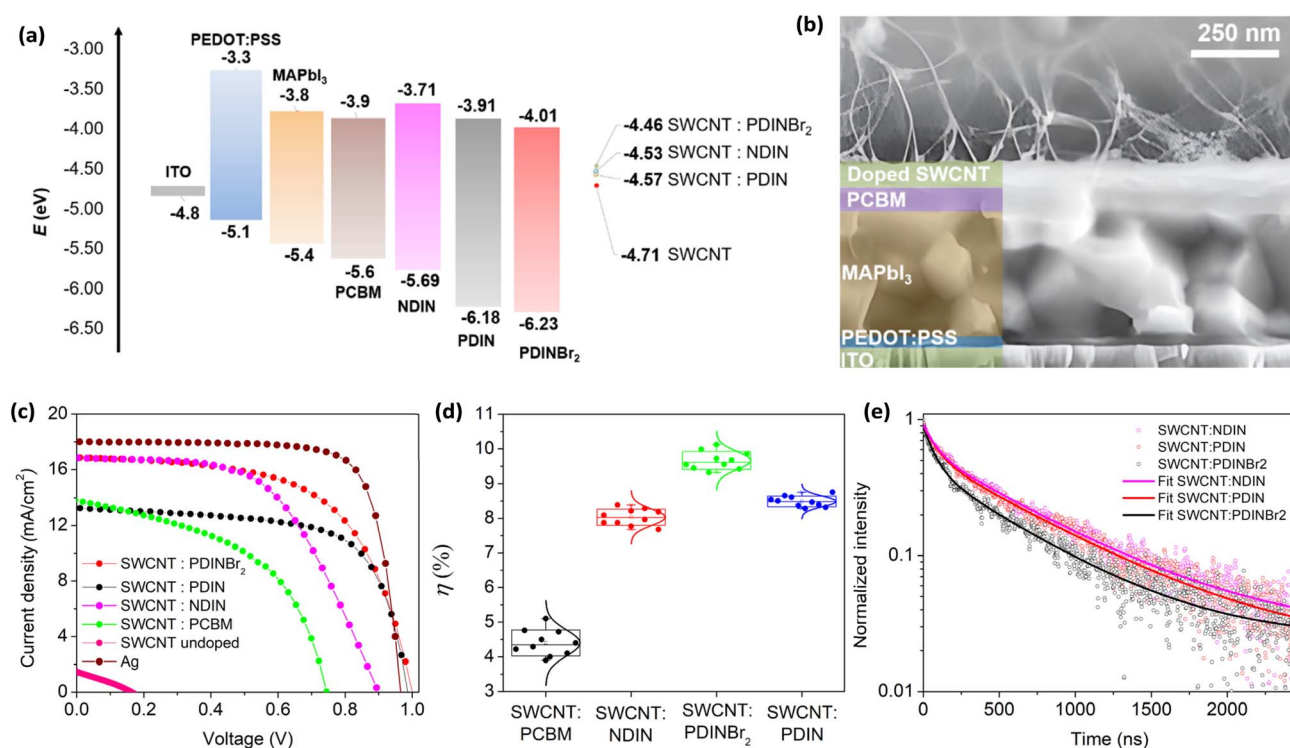

Fig. 4 (a) Energy level diagram of the inverted perovskite solar cell, (b) their cross-sectional SEM image, (c) comparison of J–V characteristics of inverted perovskite solar cells incorporating different cathodes, (d) statistical distributions of power conversion efficiency, and (e) microwave photoconductivity decay (μ-PCD) profiles of ITO/MAPbI$_3$/PCBM/n-doped SWCNT bilayers.

Table 1 Electrical properties of inverted PSCs utilizing pristine and doped SWCNT film as the electrode, where J_{SC} is the current density at zero voltage, V_{OC} is the voltage at zero current, FF is the fill factor, R_S is the series resistance, R_{Sh} is the shunt resistance, and η is the power conversion efficiency

Electrode	J_{SC} (mA cm^{-2})	V_{OC} (V)	FF	R_S (Ω cm^{-2})	R_{Sh} (Ω cm^2)	η (%)
SWCNTs:PDINBr$_2$	16.87	1.00	0.63	8.20	947.49	10.12
SWCNTs:PDIN	13.25	0.99	0.67	6.09	841.19	8.75
SWCNTs:NDIN	16.84	0.89	0.55	17.62	1740.7	8.38
SWCNTs:PCBM	13.79	0.74	0.496	9.10	195.94	5.09
SWCNTs	1.47	0.16	0.28	51.51	134.72	0.07
Ag	18.00	0.96	0.76	3.63	13 096	13.38

The J–V characteristics and distribution of the devices ($n =$ 10) incorporating different cathodes are presented in Fig. 3c, d, S6 and Table 1. Initially, devices incorporating undoped SWCNTs exhibited negligible photovoltaic performance ($\eta =$ 0.07%), primarily due to poor interfacial adhesion between the SWCNT film and the PCBM layer, as well as their intrinsic p-type nature. Although overcoating PCBM on top of the SWCNT layer improved adhesion and resulted in typical J–V characteristics, the PCE remained low ($\eta =$ 5.09%) due to the unchanged p-type characteristic of SWCNTs after PCBM overcoating.[41]

The poor performance of pristine SWCNT cathodes can be understood considering recent reports on MAPbI$_3$/CNT interfaces. Haque *et al.* showed that MAPbI$_3$ coating induces p-type doping of SWCNT networks, leading to a marked increase in their conductivity but reinforcing their hole-transporting character.[42] Likewise, MAPbI$_3$ nanowires/CNT hybrid devices exhibit strong hole transfer and photo-doping at the interface.[43] In our architecture, such perovskite-induced p-doping of pristine SWCNTs likely reduces the effective built-in potential for electron extraction and promotes recombination at the MAPbI$_3$/PCBM/SWCNT contact, contributing to the low FF and V_{OC} observed for undoped SWCNT cathodes. Introducing the n-type dopants counteracts the p-type doping effect, which can enhance the built-in potential and, in turn, improve device performance.

Incorporation of dopants into the SWCNT network successfully converted their electronic character to n-type, significantly enhancing device performance to levels comparable with Ag-based electrodes. Among the dopants tested, PDINBr$_2$-doped SWCNTs achieved the highest PCE ($\eta \approx$ 10.12%), followed by PDIN ($\eta \approx$ 8.75%) and NDIN ($\eta \approx$ 8.38%). During device optimization, we also found that the fill factors (FF) exhibit a clear maximum at an intermediate dopant loading, whereas both insufficient and excessive concentrations lead to a pronounced FF decrease (Fig. S7 and Table S2). We believe this correlated with the homogeneity and local distribution of dopants within the SWCNT film. The relatively low FF observed suggest limitations likely related to interfacial contact or charge extraction efficiency, a common challenge also reported in other studies utilizing SWCNT electrodes in PSCs.[19,21,22,44]

To assess the impact of SWCNT cathode thickness, we compared our standard electrodes ($\approx$ 35% transmittance) with thicker SWCNT films exhibiting $\approx$ 30% and 20% transmittance, while keeping the dopant concentration and treatment conditions identical. The thicker SWCNT cathodes yielded reduced

V_{OC}, J_{SC}, and overall PCE (Fig. S8). These results indicate that simply increasing CNT thickness does not guarantee higher efficiency, instead, the SWCNT thickness and dopant loading must be co-optimized to ensure homogeneous n-type conversion throughout the electrode.

The significantly enhanced device performance can be directly attributed to the fact that among the dopants PDINBr$_2$ exhibited the deepest LUMO level (-4.01 eV), ensuring the most favourable energy level alignment with PCBM that promotes efficient electron transfer. Additionally, PDINBr$_2$ showed the strongest adsorption energy (-0.91 eV), the highest induced dipole moment (2.14 D), and the greatest charge transfer to SWCNTs (0.09e) in DFT simulations, indicating strongest molecular interactions and more stable complex formation on the SWCNT surface. These theoretical findings align well with the experimental trends observed in conductivity, mobility, Seebeck coefficient, and ultimately the device performance. NDIN-doped SWCNTs showed lower performance with reduced V_{OC} and FF. This is attributed to NDIN's shallower LUMO level (-3.72 eV), leading to a weaker driving force for electron transfer from PCBM and a higher probability of interfacial recombination. NDIN's highest adsorption energy and lowest dipole moment imply less favourable electronic coupling and complex formation to SWCNTs. To investigate charge extraction behaviour and recombination dynamics in the devices, microwave photoconductivity decay (μ-PCD) measurements were conducted on ITO/MAPbI$_3$/PCBM/n-doped SWCNT films. As shown in Fig. 4e and Table S3, the photoconductivity decay profiles and their fitting results revealed differences depending on the type of dopant used in the SWCNT cathode.

The interaction between semiconducting SWCNTs and perylene or naphthalene-based dopants can significantly influence charge separation and recombination dynamics at the heterojunction interface.[45] The sample containing NDIN- and PDIN-doped SWCNT films exhibited a relatively long carrier lifetime, suggesting a slower charge extraction process and the possible accumulation of charges at the PCBM interface. Such behavior implies that while charge separation occurs efficiently, the subsequent electron transfer from PCBM to the doped SWCNT layer may be hindered, potentially due to weaker interfacial electronic coupling or suboptimal energy-level alignment.

In contrast, the PDINBr$_2$-doped SWCNT film displayed markedly faster photocarrier decay dynamics, indicating more efficient charge extraction across the heterojunction. This

accelerated decay reflects a more effective electron transfer process facilitated by PDINBr$_2$, which possesses favorable electronic coupling and stronger interfacial interactions with PCBM. Consequently, the reduced carrier lifetime in this system corresponds to diminished charge accumulation and lower recombination losses, ultimately promoting more efficient charge transport and device performance.

The PSC devices were stored under controlled temperature (25 °C), humidity (25% RH) and ambient light (300 lux) conditions for over 2000 hours, and their power conversion efficiency was periodically monitored (Fig. S8a). The degree of PCE degradation strongly correlated with the doping stability of the SWCNT cathodes. To isolate the intrinsic changes in the doped films, we simultaneously tracked S and R_{Sheet} of standalone doped SWCNT films under identical conditions (Fig. S8b and S8c). For devices employing PDIN and PDINBr$_2$-doped SWCNTs, the PCE remained relatively stable over time, with minimal decay (10%) observed after 500 hours. This was consistent with their most stable n-type Seebeck coefficient and lowest R_{Sheet}, indicating that the electronic structure and conductivity of the SWCNT film were well-preserved. Conversely, devices with NDIN-doped SWCNTs experienced faster PCE decay, particularly through significant increase in R_{Sheet}. The gradual increase in sheet resistance during storage is attributed to partial dedoping of the SWCNT network. Because the dopants are non-covalently bound, slow desorption or rearrangement of dopant molecules and competitive oxygen adsorption shift the SWCNTs back toward their intrinsic p-type state, consistent with the simultaneous increase in R_{Sheet} and the S shifting to more positive values.

From a broader perspective, approaching 20% PCE with doped CNT electrodes will require simultaneous optimization at several levels. First, the sheet resistance of CNT networks must be further reduced (for example by higher-density, partially aligned, or double-walled CNT films and hybrid CNT architecture) while maintaining high transparency, as demonstrated in high-performance CNT transparent electrodes for PSCs.[46,47] Second, rationally designed n-type dopants with stronger yet stable electron-donating ability and controlled spatial distribution are needed to minimize series resistance and FF loss, in line with recent progress on stable molecular/macromolecular n-doping of SWCNT cathodes.[48,49] Third, combining such doped CNT cathodes with state-of-the-art perovskite compositions and interface/passivation engineering, as already realized in efficient carbon-based anode PSCs approaching or exceeding 19–20% PCE, should enable further gains in V_{OC} and J_{SC}.[50–52] We believe that progress along these directions can ultimately push metal-free CNT-based cathodes in inverted PSCs toward the 20% efficiency regime.

Conclusions

This study demonstrates the effective use of perylene- and naphthalene-based planar aromatic molecules as n-type dopants for single-walled carbon nanotube (SWCNT) cathodes in inverted perovskite solar cells (PSCs). Through both experimental characterization and DFT calculations, we revealed that

the electronic properties and interfacial behavior of SWCNTs can be finely tuned via molecular doping. Among the investigated dopants, PDINBr$_2$ showed the strongest electronic coupling and optimal energy alignment, resulting in the highest device performance with a power conversion efficiency of 10.12%. The doped SWCNT electrodes enabled efficient electron extraction and contributed to improved operational stability, with perylene-based systems maintaining 80% of their initial efficiency after 800 hours of storage under controlled temperature (25 °C), humidity (25% RH) and ambient light (300 lux) conditions. These findings underscore the potential of rationally designed molecular dopants to enable scalable, flexible, and metal-free electrode architecture for high-performance perovskite photovoltaics.

Author contributions

Conflicts of interest

There are no conflicts to declare.

Data availability

The data supporting this article have been included as part of the Supplementary Information (SI). Supplementary information: detailed experimental procedures for FCCVD-grown SWCNT films, synthesis and characterization of PDINBr$_2$ and NDIN (including ^{1}H NMR), perovskite solar cell fabrication and full device/film characterization protocols; additional DFT calculation details and charge-density/PDOS analyses; supplementary Fig. (S1–S9) showing PDOS, NIR absorption, Raman spectra, SCLC mobility, dark and illuminated I–V, device statistics, J–V curves versus dopant concentration and SWCNT transmittance, and long-term stability; and supplementary Tables (S1–S7) summarizing charge-transfer analysis, full photovoltaic parameters, μ-PCD fitting results, and Cartesian coordinates of optimized molecular and SWCNT structures. See DOI: https://doi.org/10.1039/d5el00171d.

Acknowledgements

the µ-PCD measurement and SEM observation. The computation was performed using Research Center for Computational Science, Okazaki, Japan (Project: 25-IMS-C287, 24-IMS-C410).

References

1 S. Liu, V. P. Biju, Y. Qi, W. Chen and Z. Liu, *NPG Asia Mater.*, 2023, **15**, 1–28.

2 R. Azmi, E. Ugur, A. Seitkhan, F. Aljamaan, A. S. Subbiah, J. Liu, G. T. Harrison, M. I. Nugraha, M. K. Eswaran, M. Babics, Y. Chen, F. Xu, T. G. Allen, A. ur Rehman, C.-L. Wang, T. D. Anthopoulos, U. Schwingenschlögl, M. De Bastiani, E. Aydin and S. De Wolf, *Science*, 2022, **376**, 73–77.

3 J.-Y. Jeng, Y.-F. Chiang, M.-H. Lee, S.-R. Peng, T.-F. Guo, P. Chen and T.-C. Wen, *Adv. Mater.*, 2013, **25**, 3727–3732.

4 W. Chen, Y. Wu, Y. Yue, J. Liu, W. Zhang, X. Yang, H. Chen, E. Bi, I. Ashraful, M. Grätzel and L. Han, *Science*, 2015, **350**, 944–948.

5 X. Zheng, Y. Hou, C. Bao, J. Yin, F. Yuan, Z. Huang, K. Song, J. Liu, J. Troughton, N. Gasparini, C. Zhou, Y. Lin, D.-J. Xue, B. Chen, A. K. Johnston, N. Wei, M. N. Hedhili, M. Wei, A. Y. Alsalloum, P. Maity, B. Turedi, C. Yang, D. Baran, T. D. Anthopoulos, Y. Han, Z.-H. Lu, O. F. Mohammed, F. Gao, E. H. Sargent and O. M. Bakr, *Nat. Energy*, 2020, **5**, 131–140.

6 K. Domanski, J.-P. Correa-Baena, N. Mine, M. K. Nazeeruddin, A. Abate, M. Saliba, W. Tress, A. Hagfeldt and M. Grätzel, *ACS Nano*, 2016, **10**, 6306–6314.

7 L. Liang, Y. Cai, X. Li, M. K. Nazeeruddin and P. Gao, *Nano Energy*, 2018, **52**, 211–238.

8 Y. Chen, L. Zhang, Y. Zhang, H. Gao and H. Yan, *RSC Adv.*, 2018, **8**, 10489–10508.

9 T. W. Ebbesen, H. J. Lezec, H. Hiura, J. W. Bennett, H. F. Ghaemi and T. Thio, *Nature*, 1996, **382**, 54–56.

10 L. Fagiolari and F. Bella, *Energy Environ. Sci.*, 2019, **12**, 3437–3472.

11 L. Wieland, H. Li, C. Rust, J. Chen and B. S. Flavel, *Adv. Energy Mater.*, 2021, **11**, 2002880.

12 S. N. Habisreutinger, T. Leijtens, G. E. Eperon, S. D. Stranks, R. J. Nicholas and H. J. Snaith, *Nano Lett.*, 2014, **14**, 5561–5568.

13 P. G. C. Keith B, *Science*, 2000, **287**, 1801–1804.

14 B.-W. Zhang, H.-S. Lin, X.-Y. Qiu, Q.-J. Shui, Y.-J. Zheng, M. Almesfer, E. I. Kauppinen, Y. Matsuo and S. Maruyama, *Carbon*, 2023, **205**, 321–327.

15 I. Jeon, A. Shawky, S. Seo, Y. Qian, A. Anisimov, E. I. Kauppinen, Y. Matsuo and S. Maruyama, *J. Mater. Chem. A*, 2020, **8**, 11141–11147.

16 A. Elakshar, S. Tsarev, P. M. Rajanna, M. Tepliakova, L. Frolova, Y. G. Gladush, S. M. Aldoshin, P. A. Troshin and A. G. Nasibulin, *ACS Appl. Energy Mater.*, 2021, **4**, 13395–13400.

17 P. Fooladvand, M. Eskandari, D. Fathi and N. Das, *Energy Rep.*, 2023, **10**, 3652–3664.

18 H. Li, K. Cao, J. Cui, S. Liu, X. Qiao, Y. Shen and M. Wang, *Nanoscale*, 2016, **8**, 6379–6385.

19 Z. Li, S. A. Kulkarni, P. P. Boix, E. Shi, A. Cao, K. Fu, S. K. Batabyal, J. Zhang, Q. Xiong, L. H. Wong, N. Mathews and S. G. Mhaisalkar, *ACS Nano*, 2014, **8**, 6797–6804.

20 S. N. Habisreutinger, T. Leijtens, G. E. Eperon, S. D. Stranks, R. J. Nicholas and H. J. Snaith, *J. Phys. Chem. Lett.*, 2014, **5**, 4207–4212.

21 Q. Luo, H. Ma, F. Hao, Q. Hou, J. Ren, L. Wu, Z. Yao, Y. Zhou, N. Wang, K. Jiang, H. Lin and Z. Guo, *Adv. Funct. Mater.*, 2017, **27**, 1703068.

22 Y. Zhou, X. Yin, Q. Luo, X. Zhao, D. Zhou, J. Han, F. Hao, M. Tai, J. Li, P. Liu, K. Jiang and H. Lin, *ACS Appl. Mater. Interfaces*, 2018, **10**, 31384–31393.

23 H. Wang, P. Wei, Y. Li, J. Han, H. R. Lee, B. D. Naab, N. Liu, C. Wang, E. Adijanto, B. C.-K. Tee, S. Morishita, Q. Li, Y. Gao, Y. Cui and Z. Bao, *Proc. Natl. Acad. Sci. U. S. A.*, 2014, **111**, 4776–4781.

24 J. M. Gotthardt, S. Schneider, M. Brohmann, S. Leingang, E. Sauter, M. Zharnikov, H.-J. Himmel and J. Zaumseil, *ACS Appl. Electron. Mater.*, 2021, **3**, 804–812.

25 S. M. Kim, J. H. Jang, K. K. Kim, H. K. Park, J. J. Bae, W. J. Yu, I. H. Lee, G. Kim, D. D. Loc, U. J. Kim, E.-H. Lee, H.-J. Shin, J.-Y. Choi and Y. H. Lee, *J. Am. Chem. Soc.*, 2009, **131**, 327–331.

26 M. L. Geier, K. Moudgil, S. Barlow, S. R. Marder and M. C. Hersam, *Nano Lett.*, 2016, **16**, 4329–4334.

27 V. Schroeder, S. Savagatrup, M. He, S. Lin and T. M. Swager, *Chem. Rev.*, 2019, **119**, 599–663.

28 T. Song, X. Zhang, C. Xie and P. Yang, *Carbon*, 2023, **210**, 118052.

29 L. Gao, H. Wang, Q. Guo, Z. Wang, F. Yuan and E. Zhou, *Chem. Eng. J.*, 2024, **480**, 148277.

30 Z. Wang, H. Wang, L. Yang, M. Du, L. Gao, Q. Guo and E. Zhou, *Angew. Chem., Int. Ed.*, 2024, **63**, e202404921.

31 Z. Wang, H. Wang, M. Du, X. Lai, F. He, Q. Guo, Q. Guo, A. Tang, X. Sun and E. Zhou, *Adv. Funct. Mater.*, 2024, **34**, 2313240.

32 C. Backes, C. D. Schmidt, F. Hauke, C. Böttcher and A. Hirsch, *J. Am. Chem. Soc.*, 2009, **131**, 2172–2184.

33 B. Russ, M. J. Robb, F. G. Brunetti, P. L. Miller, E. E. Perry, S. N. Patel, V. Ho, W. B. Chang, J. J. Urban, M. L. Chabinyc, C. J. Hawker and R. A. Segalman, *Adv. Mater.*, 2014, **26**, 3473–3477.

34 C. Ehli, C. Oelsner, D. M. Guldi, A. Mateo-Alonso, M. Prato, C. Schmidt, C. Backes, F. Hauke and A. Hirsch, *Nat. Chem.*, 2009, **1**, 243–249.

35 J. Calbo, A. Doncel-Giménez, J. Aragó and E. Ortí, *Theor. Chem. Acc.*, 2018, **137**, 27.

36 M. C. R. Delgado, E.-G. Kim, D. A. da S. Filho and J.-L. Bredas, *J. Am. Chem. Soc.*, 2010, **132**, 3375–3387.

37 F. Yang, L. Dong, D. Jang, K. C. Tam, K. Zhang, N. Li, F. Guo, C. Li, C. Arrive, M. Bertrand, C. J. Brabec and H.-J. Egelhaaf, *Adv. Energy Mater.*, 2020, **10**, 2001869.

38 Z. Chen, H. Zhang, F. Yao, C. Tao, G. Fang and G. Li, *Cell Rep. Phys. Sci.*, 2020, **1**, 100205.

39 H. Lu, A. Krishna, S. M. Zakeeruddin, M. Grätzel and A. Hagfeldt, *iScience*, 2020, **23**, 101359.

40 J.-W. Lee, S. Tan, S. I. Seok, Y. Yang and N.-G. Park, *Science*, 2022, **375**, eabj1186.

41 C. Delacou, I. Jeon, K. Otsuka, T. Inoue, A. Anisimov, T. Fujii, E. I. Kauppinen, S. Maruyama and Y. Matsuo, *InfoMat*, 2019, **1**, 559–570.

42 M. A. Haque, T. Yu, H. Choubisa, L. H. Hernandez, Y. Zhou, A. Genovese, B. Davaasuren, C. Combe, H. Li, J. M. Luther, J. L. Blackburn, E. H. Sargent, W.-L. Ong and D. Baran, *Adv. Sci.*, 2025, **12**, e07589.

43 M. Spina, B. Náfrádi, H. M. Tóháti, K. Kamarás, E. Bonvin, R. Gaal, L. Forró and E. Horváth, *Nanoscale*, 2016, **8**, 4888–4893.

44 S. N. Habisreutinger, T. Leijtens, G. E. Eperon, S. D. Stranks, R. J. Nicholas and H. J. Snaith, *Nano Lett.*, 2014, **14**, 5561–5568.

45 H. S. Kang, T. J. Sisto, S. Peurifoy, D. H. Arias, B. Zhang, C. Nuckolls and J. L. Blackburn, *J. Phys. Chem. C*, 2018, **122**, 14150–14161.

46 S. N. Habisreutinger and J. L. Blackburn, *J. Appl. Phys.*, 2021, **129**, 010903.

47 X.-G. Hu, Z. Lin, L. Ding and J. Chang, *SusMat*, 2023, **3**, 639–670.

48 A. S. Hidayat, N. Ueoka, M. Shimamoto, M. Huda, H. Oshima, Y. Hijikata, A. Muraoka, Y. Nonoguchi and Y. Matsuo, *J. Mater. Chem. A*, 2025, **13**, 42142–42151.

49 N. Ueoka, A. S. Hidayat, H. Oshima, Y. Hijikata and Y. Matsuo, *ACS Appl. Mater. Interfaces*, 2025, **17**, 64796–64807.

50 H. Xie, J. Lei, Z. Zhu, X. Xu, D. Li, J. Xu, Y. Pan and X. Yin, *ACS Appl. Mater. Interfaces*, 2025, **17**, 33271–33295.

51 T. Du, S. Qiu, X. Zhou, V. M. L. Corre, M. Wu, L. Dong, Z. Peng, Y. Zhao, D. Jang, E. Spiecker, C. J. Brabec and H.-J. Egelhaaf, *Joule*, 2023, **7**, 1920–1937.

52 L. Luo, J. Gu, Y. Shen, S. Li, S. Chen, Y. Yang, B. Li, Y. Rong, X. Li and J. Ding, *Renew. Sustain. Energy Rev.*, 2026, **226**, 116474.